

## Be-ion implanted $p$ - $n$ InSb diode for infrared applications. Modeling, fabrication and characterization

V.V. Koroteyev\*, V.O. Kochelap, S.V. Sapon, B.M. Romaniuk, V.P. Melnik, O.V. Dubikovskiy, T.M. Sabov

Department of Theoretical Physics

V. Lashkaryov Institute of Semiconductor Physics, 41, prospect Nauky, 03680 Kyiv, Ukraine

\* E-mail: koroteev@ukr.net

**Abstract.** Transport theory for modeling the electric characteristics of high-quality  $p$ - $n$  diodes has been developed. This theory takes into account a non-uniform profile of  $p$ -doping, finite thickness of the quasi-neutral regions and possible non-uniformity of the bulk recombination coefficient. The theory is based on related solutions of the Poisson equation, drift-diffusion equation and continuity equation with a generation-recombination term taking into account the simple band-to-band generation/recombination model. We have ascertained that the non-uniform profile of  $p$ -doping can lead to formation of  $p$ - $n$  junctions with a specific two-slope form of the electrostatic barrier and two regions with the high built-in electric fields. We have found that at strong  $p^+$ -doping the band structure of the InSb  $p$ - $n$  junction has the form that can facilitate the emergence of additional mechanisms of current flow due to the tunneling and avalanche effects at the reverse bias. Using the literary data of the electron and hole lifetimes in InSb at cryogenic temperatures, we have found that the coefficient of bulk recombination can have an essential spatial dependence and considerably increases in the space charge region of  $p$ - $n$  diode. The theory was applied to our analysis of  $p$ - $n$  InSb diodes with  $p^+$ -doping by using Be-ion implantation performed in ISP NASU. The theory predicts optimal conditions for detection of infrared emission. The technological process of fabrication, processing and testing has been described in details. Theoretically, it has been found that for parameters of the fabricated diodes and at 77 K the dark currents limited by diffusion and generation-recombination mechanisms should be less than 0.1  $\mu$ A at the inverse bias of the order of 0.1 V. The measured diode's  $I$ - $V$  characteristics were expected to have strong asymmetry, however, dark currents are by one order larger than those predicted by theory. The latter can be associated with additional current mechanisms, namely: tunneling and avalanche effects.

**Keywords:**  $p$ - $n$  diode, ion implantation, InSb.

doi: <https://doi.org/10.15407/spqeo21.03.294>

PACS 61.72.uj, 85.30.Kk

Manuscript received 13.09.18; revised version received 28.09.18; accepted for publication 10.10.18; published online 22.10.18.

### 1. Introduction

Nowadays, narrow bandgap semiconductor compounds like to indium antimonide (InSb) and  $\text{Cd}_x\text{Hg}_{1-x}\text{Te}$  alloy still remain the actual and key elements for modern infrared (IR) technologies [1, 2]. These technologies are oriented on the development of efficient photodetectors for different applications, including IR imaging system, short range communication, security system, atomic and molecular spectroscopies, biochemical sensors, astronomy and civil space applications, military applications, *etc.* [3]. Within the actual IR range, there are two important bands 3...5 and 8...12  $\mu\text{m}$ , which are referred to as mid-wave IR (MWIR) and long-wave (LWIR), respectively. They correspond to absorption

minima in the atmosphere. Indeed, InSb remains the most used material for MWIR imaging, showing a cut-off wavelength at 5.5  $\mu\text{m}$  at 77 K, because the InSb band structure is favorable for fabrication of efficient IR photodetectors.

Intensive studies of physical properties of InSb started from 60-es of the past century. These studies were focused on both experimental and theoretical researches of important characteristics, namely: electron and hole mobilities [4, 5], electron and holes lifetimes [6, 7], including the detail studies of recombination mechanisms [8-10], optical characterization of the band structure [11], *etc.* Information about basic parameters of InSb is summarized in several recent handbooks [12, 13].

The most popular version of electronic IR

photodetectors is the  $p$ - $n$  diodes made from narrow bandgap materials. Their operation principle is based on the photoconductive effect that provides an ultimate sensitivity of the diode's current voltage ( $I$ - $V$ ) characteristic to the external illumination. The InSb infrared photodiodes operating at 77 K are commonly fabricated by standard planar method, where the  $p$ - $n$  junction is formed by ion implantation of  $p$ -type impurities on one side of an InSb bulk substrate. Different types of the ion implanted impurities, are discussed, for example, protons [14], Mg [15], Zn [16] and Be [17, 18]. In spite of some obstacles (ion implantation can damage surface and produces a troublesome porous surface layer that is not annealed out, even at the melting temperature of InSb, and which was difficult to remove by dissolution [15]), ion implantation remains the most cheap and simplest technique for mass production of IR photodetectors.

Besides the  $p$ - $n$  diode, other types of opto-electronic devices were proposed. And among them, the avalanche photodiodes should be noted [19] (where the impact ionization properties of carriers are used), quantum well [20] and quantum dot [21] infrared photodetectors. Two latter examples exploit the mechanism of intersubband excitations in quantum heterostructures with artificially engineered band structure [22, 23]. These photodiodes have a much narrower wavelength response compared to that of bulk materials. However, they require the expensive growth technologies. Further improvement of the photodetector performance is associated with application of special coating in the form of plasmonic or photonic crystals, which enhances the coupling of the electronic device with incident radiation [24, 25].

This paper is devoted to detail investigations of the Be-ion implanted  $p$ - $n$  InSb diode fabricated in Labs of ISP NASU. These studies include the theoretical modeling of the physical processes in the diode, calculation of electric characteristics, description of technological aspects of fabrication and, finally, electrical measurements.

It should be emphasized that correct modeling and quantitative analysis of the electron transport through the  $p$ - $n$  junction is a very complicated problem because of the existence of different mechanisms of current transport, which contribute differently to the total  $I$ - $V$  characteristic depending on parameters and quality of the  $p$ - $n$  junction. Among these mechanisms, there are bulk and surface diffusion currents, bulk and surface generation-recombination currents, band-to-band and impurity-assisted tunneling currents [26-28]. Besides, the effect of carrier avalanche multiplication can also occur [19]. The existing analytical transport models that give the general behavior of  $I$ - $V$  dependences have a number of restrictions for applicability. They are developed for simplified situations, assuming abrupt doping profiles, nondegenerate carriers or using the approximation of short or long depletion regions. The more rigorous calculations face with the difficulties of the numerical solutions of corresponding equations (typically, it is drift-diffusion models with corresponding boundary

conditions). These difficulties are associated with the existence of large parameters (ratio of widths of  $n$ - and  $p$ -doped regions to the corresponding Debye radii) in the corresponding differential equations. Therefore, the numerical simulation of the diodes with wide quasi-neutral regions and relatively short space charge region faces with the problem of different functional dependences of electric characteristics vs coordinates: very smooth behavior in the quasi-neutral regions and sharp behavior in the space charge region. To overcome these numerous obstacles, it is often used advent commercial device simulators with specific choice of the non-uniform grid to realize calculations by using finite-element schemes [19, 29, 30].

In this paper, to study electric characteristics of a  $p$ - $n$  diode, we used original computational algorithms and the proper developed software. The transport model, basic equations and analysis of the obtained electric characteristics for the sample with modeling parameters are presented in Sections 2 and 3. Then, the developed theoretical approaches were applied to calculate the  $I$ - $V$  characteristics of fabricated  $p$ - $n$  diode. The details of this fabrication are discussed in Section 4. The comparison and analysis of the calculated and measured  $I$ - $V$  characteristics are given in Section 5. Section 6 summarizes the basic results and contains discussion of further directions of investigations.

## 2. Theoretical model and electrostatics of the $p$ - $n$ junction (rigorous calculations)

Let us assume the InSb sample with inter-contact distance,  $L$ , along  $x$ -axis. The theory is developed for the case of the 1D consideration of the electron transport, which implies that other dimensions of the samples are much greater with respect to  $L$ . The sample is uniformly low-doped with  $n$ -type Te donor impurities. The donor concentration is assumed to be  $N_d$ , and all donor states are ionized. The latter is realized for Te donors even at nitrogen temperature [12, 31]. In order to create the  $p$ - $n$  junction, for instance, the right part of the sample should be heavily-doped by  $p$ -type Be impurities with some distribution  $N_a(x)$ . The Be impurities as well as other II-group elements are the shallow acceptors in the InSb [4]. In the model, all acceptor levels will be also considered as the ionized ones.

The modeling of electric characteristics of the InSb  $p$ - $n$  diode begins from the equilibrium case. Calculations of the equilibrium electrostatic characteristics, such as spatial distributions of the built-in electrostatic energy (potential profile), electric field, electron and hole concentrations, *etc.*, are reduced to the solution of the Poisson equation:

$$\frac{d^2\phi(x)}{dx^2} = \frac{4\pi e}{\kappa_0} [n(x) - N_d - p(x) + N_a(x)], \quad (1)$$

where  $\phi(x)$  is the electrostatic potential,  $e$  – elementary charge, and  $\kappa_0$  being the static dielectric permittivity. The Poisson equation (1) should be supplied by

definition of electron,  $n(x)$ , and hole,  $p(x)$ , concentrations. In the case of the arbitrary degeneracy of carriers, the latter quantities can be expressed in terms of the special function – Fermi–Dirac integral of  $1/2$  order,  $F_{1/2}(x)$  [32]:

$$\begin{aligned} n(x) &= N_c F_{1/2}[(\varepsilon_F + e\phi(x))/k_B T], \\ p(x) &= N_v F_{1/2}[(-\varepsilon_F - \varepsilon_g - e\phi(x))/k_B T]. \end{aligned} \quad (2)$$

Here,  $N_{c,v} = 2^{1/2} m_{c,v}^{3/2} (k_B T)^{3/2} / \pi^2 \hbar^3$  are the effective densities of states in the conduction (c) and valence (v) bands, respectively,  $m_c$  – electron effective mass,  $m_v$  – hole effective mass of density of states,  $\hbar$  – Dirac constant and  $T$  – ambient temperature. Eqs. (2) were obtained under assumption of the parabolic dispersion law of carriers, where  $\varepsilon_g$  is the bandgap between conduction and valence bands. At the equilibrium, the Fermi level,  $\varepsilon_F$ , should be constant across the whole sample.

Eq. (1) together with Eqs. (2) form the non-linear differential equation of the second order, which in the dimensionless variables can be written as follows:

$$\frac{d^2 \Phi(X)}{dX^2} = -[N'_c F_{1/2}(\xi_F - \Phi) - 1 - N'_v F_{1/2}(\Phi - \xi_F - \xi_g) + R_0 r(X)] \equiv \rho'(X), \quad (3)$$

where  $\Phi = -e\phi/k_B T$ ,  $\xi_{F,g} = \varepsilon_{F,g}/k_B T$ ,  $N'_{c,v} = N_{c,v}/N_d$  and  $R_0 = N_a/N_d$  (here  $N_a$  denotes the maximal value of acceptor concentration). The quantity  $\rho'(X)$  has the meaning of the dimensionless total charge density. The dimensionless profile of the  $p$ -doping,  $r(X)$ , is the function of the dimensionless coordinate,  $X = x/L_D$ , which is scaled on characteristic Debye radius of electrons in the  $n$ -doped region of the sample,

$L_D = \sqrt{\kappa_0 k_B T / 4\pi e^2 N_d}$ . Solution of Eq. (3) requires specification of the boundary conditions and determination of Fermi level,  $\xi_F$ . Without loss of generality, we apply that

$$\Phi(-L'_n) = 0, \quad \Phi(L'_p) = \Phi_b, \quad (4)$$

where  $L'_{n,p}$  are the dimensionless coordinates of the left and right ends of the sample (interfaces between InSb and contacts).  $\Phi_b$  is the height of the built-in electrostatic barrier. In our model, we assumed that contacts are Ohmic, and ones sustain the charge neutrality in such a manner that the total charge density,  $\rho'(X)$ , is equal to 0 at  $X = L'_n, L'_p$ . Thus,  $\xi_F$  and  $\Phi_b$  can be determined as the solutions of two non-linear algebraic equations:

$$\begin{aligned} \rho'(-L'_n) &\equiv -[N'_c F_{1/2}(\xi_F) - 1 - N'_v F_{1/2}(-\xi_F - \xi_g) + R_0 r(-L'_n)] = 0, \end{aligned} \quad (4a)$$

$$\begin{aligned} \rho'(L'_p) &\equiv -[N'_c F_{1/2}(\xi_F - \Phi_b) - 1 - N'_v F_{1/2}(\Phi_b - \xi_F - \xi_g) + R_0 r(L'_p)] = 0. \end{aligned} \quad (4b)$$

The joint solution of Eqs.(3) and (4) allows us to find all electrostatic characteristics of the  $p$ - $n$  diode under equilibrium conditions, when taking into account an

arbitrary degree of carrier degeneracy and non-uniform profile of  $p$ -doping. The proposed model of the  $p$ - $n$  junction is more general in contrast to the simplified models discussed in many textbooks [for example, see Refs. 32, 33]. Unfortunately, for the case of arbitrary form of the profile,  $r(x)$ , the formulated system of equations has no simple analytical solutions. It should be solved only numerically as a boundary-value problem (BVP) for non-linear ordinary differential equations (3) with  $\xi_F$  and  $\Phi_b$  that should be found from Eqs. (4a) and (4b).

For the solution of BVP, we used the finite-difference method which reduces Eq. (3) to the system of the non-linear algebraic equations. The latter can be solved using the Newton method with step control. The briefly described procedure has been realized in the form of the working subroutine in Fortran-source libraries.

However, successful implementation of the computations strongly depends on the choice of the initial guess of potential profile. We checked that for the case of the monotonic profile,  $r(x)$ , good initial estimation can be given by the form of potential profile obtained for the abrupt (step-like)  $p$ -doping profile,  $r(X) = \theta(X)$  (where  $\theta(X)$  denotes the Heaviside step function). Moreover, at  $r(X) = \theta(X)$  the solutions of Eq. (3) can be found analytically by quadratures.

### 2.1. Step-like $p$ -doping profile

To model the step-like doping profile, we used Eq. (3) that belongs to the class of second-order differential equations with independent variable missing. Indeed, Eq. (3) can be rewritten in the form of two first-order differential equations:

$$\frac{d(E'^-)}{d\Phi} = 2\rho'^-(\Phi), \quad 0 \leq \Phi \leq \Phi_i, \quad (5a)$$

$$\frac{d(E'^+)}{d\Phi} = 2\rho'^+(\Phi), \quad \Phi_i \leq \Phi \leq \Phi_b, \quad (5b)$$

where  $E' \equiv d\Phi/dX$  is the dimensional electrical field in the units of Debye field  $E_d = k_B T / eL_d$ , superscripts  $\mp$  designate quantities related to the regions,  $X < 0$  and  $X > 0$ , respectively, electrostatic potential at the interface,  $\Phi_i \equiv \Phi(0)$ , and total charge densities are  $\rho'^-(\Phi) = -[N'_c F_{1/2}(\xi_F - \Phi) - 1 - N'_v F_{1/2}(\Phi - \xi_F - \xi_g)]$  and

$$\rho'^+(\Phi) = -[N'_c F_{1/2}(\xi_F - \Phi) - 1 - N'_v F_{1/2}(\Phi - \xi_F - \xi_g) + R_0].$$

The solutions of Eqs. (5a) and (5b), which satisfy the boundary conditions,  $E'^-(-L'_n) = E'_L$  and  $E'^+(L'_p) = E'_R$  (note, in the case of the bounded sample, fields are not zero) can be written as follows:

$$E'^- = \left[ E_L'^2 + 2 \int_0^\Phi d\Phi' \rho'^-(\Phi') \right]^{1/2}, \quad 0 \leq \Phi \leq \Phi_i, \quad (6a)$$

$$E'^+ = \left[ E_R'^2 + 2 \int_{\Phi_b}^{\Phi} d\Phi' \rho'^+(\Phi') \right]^{1/2}, \quad \Phi_i \leq \Phi \leq \Phi_b. \quad (6b)$$

Having, the formulae 6(a) and 6(b), the spatial distribution of the potential profile can be obtained in the form of the implicit functions:

$$X = -L'_n + \int_0^{\Phi} \frac{d\Phi'}{E'^-(\Phi')} \quad 0 \leq \Phi \leq \Phi_i \quad (X < 0), \quad (6c)$$

$$X = L'_p + \int_{\Phi_b}^{\Phi} \frac{d\Phi'}{E'^+(\Phi')} \quad \Phi_i \leq \Phi \leq \Phi_b \quad (X > 0). \quad (6d)$$

Three entered unknown parameters  $E'_L$ ,  $E'_R$  and  $\Phi_i$  should be determined from the requirements of the continuity of electric field and potential at the interface,  $X = 0$ :

$$\begin{cases} E'_L{}^2 + 2 \int_0^{\Phi_i} d\Phi' \rho'^-(\Phi') = E_R'^2 + 2 \int_{\Phi_b}^{\Phi_i} d\Phi' \rho'^-(\Phi') \\ -L'_n + \int_0^{\Phi_i} \frac{d\Phi'}{E'^-(\Phi')} = 0 \\ L'_p + \int_{\Phi_b}^{\Phi_i} \frac{d\Phi'}{E'^+(\Phi')} = 0 \end{cases}$$

The solutions of nonlinear algebraic system of equations (6e) can be found numerically.

Thus, the sequential solution of the (4a), (4b) and (6e) with further tabulation of 6(c), 6(d), 6(a), 6(b) and (2) finalizes the search of equilibrium electrostatic characteristics, including spatial distributions of the potential, electric field, carrier concentrations and total built-in charge for the case of  $p$ - $n$  diode with step-like  $p$ -doping profile. After obtaining these functions, we can numerically solve BVP (Eqs. (3) and (4)) for any monotonic profile  $r(x)$ .

If the contacts are placed far from the space charge region, in the depth of the quasi-neutral regions ( $L'_{n,p} \gg 1$ ), the simpler model of the unbounded sample can be successfully used to determine the initial guess for the assumed electrostatics problem. In the frames of this model, the spatial profiles of the electric fields and potential energy are given implicitly by the formulae (7(a), 7(b)) and (7(c), 7(d)), respectively.

$$E'^- = \left[ 2 \int_0^{\Phi} d\Phi' \rho'^-(\Phi') \right]^{1/2}, \quad 0 \leq \Phi \leq \Phi_i, \quad (7a)$$

$$E'^+ = \left[ 2 \int_{\Phi_b}^{\Phi} d\Phi' \rho'^+(\Phi') \right]^{1/2}, \quad \Phi_i \leq \Phi \leq \Phi_b, \quad (7b)$$

$$X = \int_{\Phi_i}^{\Phi} \frac{d\Phi'}{E'^-(\Phi')}, \quad 0 \leq \Phi \leq \Phi_i, \quad (7c)$$

$$X = \int_{\Phi_i}^{\Phi} \frac{d\Phi'}{E'^+(\Phi')}, \quad \Phi_i \leq \Phi \leq \Phi_b. \quad (7d)$$

## 2.2. Smooth doping profile and results of calculations

The developed procedure is illustrated by the calculations of equilibrium electrostatic characteristics of the InSb  $p$ - $n$  diode with the following model parameters:  $N_a = 10^{17} \text{ cm}^{-3}$ ,  $N_d = 10^{15} \text{ cm}^{-3}$  ( $R_0 = 100$ ),  $T = 77 \text{ K}$ . In this case, the Debye radius  $L_D = 0.075 \mu\text{m}$ , and Debye field  $E_d = 0.85 \text{ kV/cm}$ . The  $p$ -doping profile is assumed to be given by the model function  $r(x) = [\tanh(\alpha X) + 1] / [\tanh(\alpha L'_p) + 1]$  with some parameters,  $\alpha$ , that describes the abruptness of the  $p$ -doping profile. Note, at  $\alpha \rightarrow \infty$ ,  $r(x) \rightarrow \theta(x)$ . The results of calculations for the electrostatic characteristics are shown in Figs. 1a to 1d. We considered three forms of the smooth  $p$ -doping profile calculated at  $\alpha = 2, 1, 0.5$  (see inset in Fig. 1a). For comparison, the results for the step-like  $p$ -doping profiles are also shown.

As seen, for the case of  $N_a \gg N_d$  and step-like profile of  $r(x)$  the space charge region is mainly formed to the left from  $n$ - $p$  interface with the typical width of  $10L_D$  ( $\sim 1 \mu\text{m}$ ). The height of the electrostatic barrier  $\Phi_b$  is approximately equal to 20, which corresponds to 0.13 V. Due to spatial redistribution of electrons and holes, the strong built-in electric field with amplitude close to  $10E_d$  ( $\sim 8 \text{ kV/cm}$ ) occurs at the interface,  $X = 0$  (see dashed curve in Fig. 1b). Two quasi-neutral regions are formed beyond the interface at  $X < -10$  ( $n$ -doped) and  $X > 0.5$  ( $p$ -doped). In these regions, the concentrations of electrons and holes are almost equal to the donor,  $N_d$ , and acceptor,  $N_a$ , concentrations, respectively. The Fermi level lies inside the bandgap, and it passes at the distance of several  $k_B T$  below the bottom of the conduction band in the  $n$ -region and above of several  $k_B T$  with respect to the top of the valence band in the  $p$ -region. As seen from Fig. 1c, the minor charge carrier concentrations (electrons in the depth of  $p$ -region and holes in the depth of  $n$ -regions) are 10 orders less than the respective major charge carrier concentrations (electrons in the depth of  $n$ -region and holes in the depth of  $p$ -regions). The total charge density distribution (Fig. 1d) is positive left from interface and negative right from interface. Moreover, the specific plateau is clearly seen in the region of  $X = -5 \dots -1$ . The emergence of this plateau corresponds to the absence of the mobile carriers of both signs (totally depleted region or Schottky layer).

The curves 1-3 demonstrate effects of smoothing in the  $p$ -doping profile. With decreasing the parameter  $\alpha$ , the width of space charge region essentially increases. The potential profile acquires the two-slope form. The observed maximum of the built-in electrostatic field is shifted to the  $n$ -region with decreasing its amplitude. So, for  $\alpha = 0.5$ , the electric field reaches the value of  $4E_d$  ( $\sim 3 \text{ kV/cm}$ ) at  $X = -5$ . Also, at  $\alpha = 0.5$ , the weak sign of the second maximum formation is observed near the  $n$ - $p$

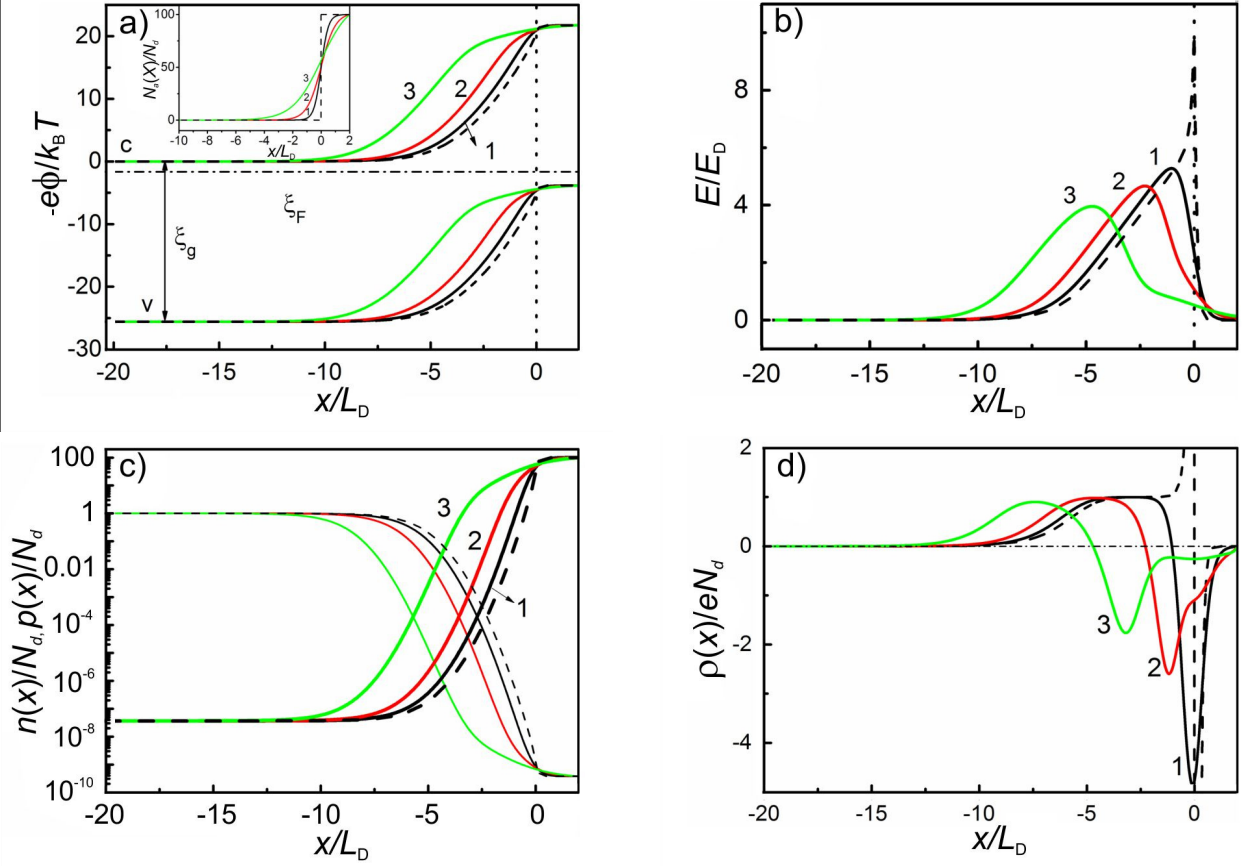


**Fig. 1.** Panels show equilibrium spatial distributions of the electrostatic energy (a), electric field (b), electron (thin lines) and hole (thick lines) concentrations (c), and total charge density (d). The curves 1, 2, 3 correspond to the parameter  $\alpha = 2, 1, 0.5$  describing the form of  $p$ -doping profile (inset in (a)). The dashed curves correspond to the case of the step-like profile,  $r(x)$ . Horizontal dash-dotted line in the panel (a) depicts the position of the Fermi level. In all the calculations, dimensionless coordinates of the contacts are assumed to be  $L'_n = -20$ ,  $L'_p = 2$ .

interface. The total charge density distribution does not show characteristic plateau (curve 3 in Fig. 1d). In this case, the positively and negatively charged regions are essentially shifted to the left part of the sample.

To finalize this section, we will briefly consider the case of the heavy  $p^+$ -doped profile, assuming  $N_a = 10^{17} \text{ cm}^{-3}$ . In this case,  $R_0 = 500$ . Calculations were performed for smooth profile  $r(x)$  with  $\alpha = 0.5$  and the same other parameters. Figs. 2a to 2d demonstrate for comparison two cases  $N_a = 10^{17} \text{ cm}^{-3}$  and  $N_a = 5 \cdot 10^{17} \text{ cm}^{-3}$ .

As expected, the increase of  $p$ -doping concentration leads to the increase of  $\Phi_b$  as well as broadening the space charge region. At higher  $p$ -doping concentrations, the hole gas in the  $p$ -region becomes degenerate. The position of the Fermi level almost coincides with the top of the valence band in the  $p$ -region. Also, the well-pronounced decrease in the minor electron carrier concentrations is observed (Fig. 2c). The distribution of total charge density shows formation of two positively-charged regions (curve 1 in Fig. 2d), which corresponds to formation of the non-monotonic distribution of the electric field with two shoulders (curve 1 in Fig. 2b).

### 3. Theoretical model of biased $p$ - $n$ diode and $I$ - $V$ characteristics

Let's the external steady-state voltage,  $U_D$ , is applied to the Ohmic contacts of  $p$ - $n$  diode. Without loss of generality, we assume that the left contact keeps the zero potential. The forward biased diode corresponds to the case of  $U_D > 0$ , when the built-in electrostatic barrier is decreased. The reverse biased diode corresponds to the case of  $U_D < 0$ , *i.e.*, the external field increases the height of the built-in electrostatic barrier. The proposed theoretical model of the carrier transport is based on joint solution of the Poisson equation (8a), equations for electron,  $j_n$ , and hole,  $j_p$ , current densities (8b and 8c) written in the frames of the drift-diffusion model, and continuity equations (8d). From the continuity equations, it immediately follows that the total current density,  $j$ , should be constant across the whole diode (Eq. (8e)):

$$\frac{d^2\phi(x)}{dx^2} = \frac{4\pi e}{\kappa_0} [n(x) - N_d - p(x) + N_a(x)], \quad E(x) = -\frac{d\phi}{dx}; \quad (8a)$$

$$j_n(x) = e\mu_n n(x)E(x) + eD_n \frac{dn(x)}{dx}; \quad (8b)$$

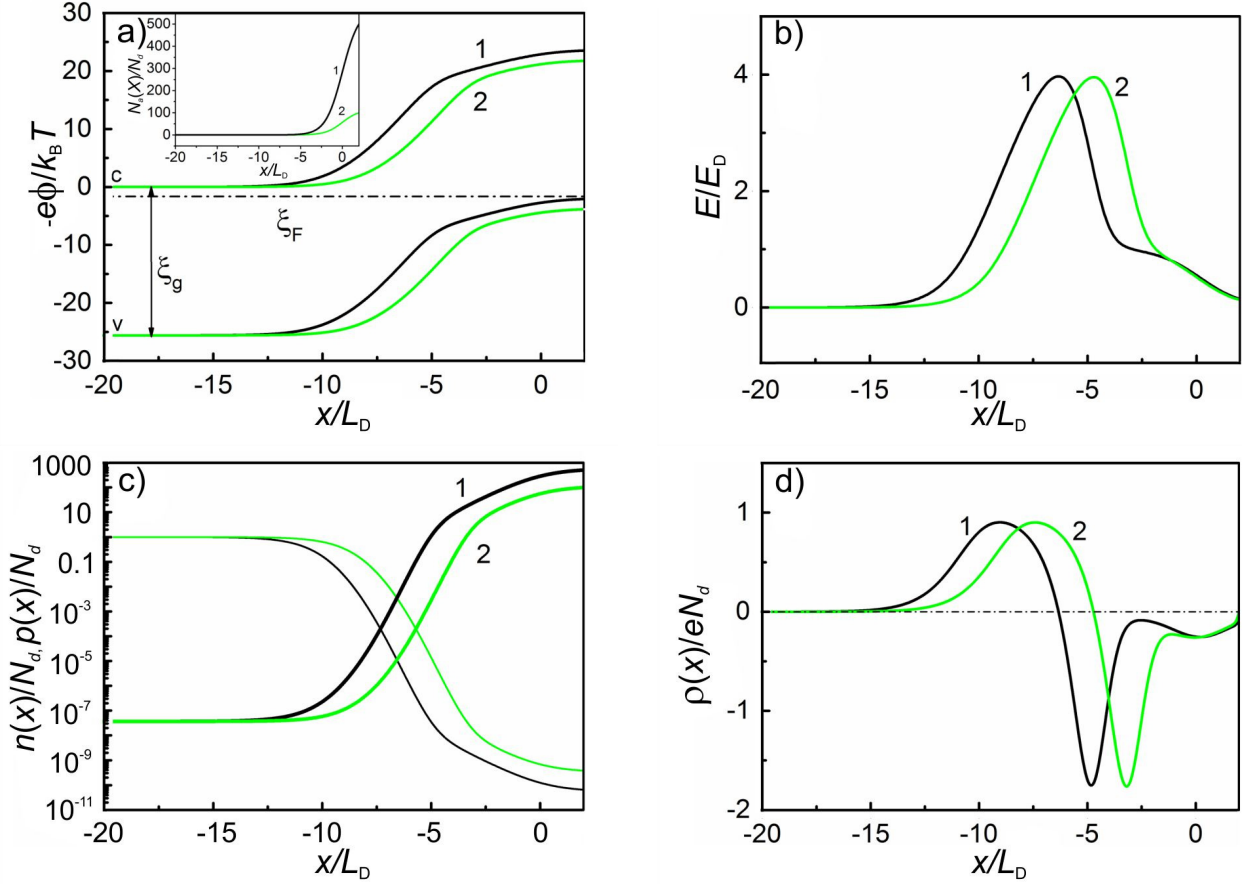


**Fig. 2.** Panels show the equilibrium spatial distributions of the same characteristics as in Fig. 1 at two different values of  $N_a$ :  $5 \cdot 10^{17} \text{ cm}^{-3}$  (1) and  $1 \cdot 10^{17} \text{ cm}^{-3}$  (2). The forms of the corresponding  $p$ -doping profiles are shown in the inset to the panel (a).

$$j_p(x) = e\mu_p p(x)E(x) - eD_p \frac{dp(x)}{dx}; \quad (8c)$$

$$\frac{1}{e} \frac{dj_n(x)}{dx} = -(G^+(x) - G^-(x)), \quad \frac{1}{e} \frac{dj_p(x)}{dx} = (G^+(x) - G^-(x)); \quad (8d)$$

$$j \equiv j_n(x) + j_p(x) = \text{const}. \quad (8e)$$

In Eqs. (8b) and (8c),  $\mu_{n,p}$  and  $D_{n,p}$  are the mobility and diffusion coefficient of electrons and holes, respectively, and they are assumed to be constant across the whole diode. It should be noted that out of equilibrium ( $U_D \neq 0$ ) the electron and hole concentrations are described by the proper quasi-Fermi levels  $\varepsilon_n(x)$  and  $\varepsilon_p(x)$  that are functions of the coordinate, *i.e.*,

$$n(x) = N_c F_{1/2} \left[ \frac{(\varepsilon_n(x) + e\phi(x))}{k_B T} \right],$$

$$p(x) = N_v F_{1/2} \left[ \frac{-\varepsilon_p(x) - \varepsilon_g - e\phi(x)}{k_B T} \right].$$

The terms  $G^\pm$  introduced to the continuity Eq. (8d) correspond to generation of electron-hole pairs and their recombination, respectively. In this section, we apply the direct generation-recombination model. In this model,  $G^+(x) - G^-(x) = -\gamma[n(x)p(x) - n_0 p_0]$  [see Ref. 32] with  $\gamma$  being the coefficient of bulk recombination, which has the dimension  $\text{cm}^3/\text{s}$ ,  $n_0$  and  $p_0$  are the equilibrium electron and hole concentrations, respectively. Further, it is convenient to express the electron and hole current densities in the terms of spatial derivatives of quasi-

Fermi levels  $d\varepsilon_n(x)/dx$  and  $d\varepsilon_p(x)/dx$  as follows:

$$j_n = n(x)\mu_n d\varepsilon_n(x)/dx \quad \text{and} \quad j_p = p(x)\mu_p d\varepsilon_p(x)/dx.$$

These formulae are the result of the Einstein relation between diffusion coefficient and mobility, which reads for electrons and holes with arbitrary degeneracy as:

$$D_n/\mu_n = k_B T / e \times [1/n(\zeta^*) \times dn(\zeta^*)/d\zeta^*]^{-1} \quad \text{and}$$

$$D_p/\mu_p = k_B T / e \times [1/p(\eta^*) \times dp(\eta^*)/d\eta^*]^{-1},$$

respectively. The variables  $\zeta^*$  and  $\eta^*$  are the dimensionless electron and hole chemical potentials, respectively,

$$\zeta^* = (\varepsilon_F + e\phi(x))/k_B T \quad \text{and} \quad \eta^* = (-\varepsilon_F - \varepsilon_g - e\phi(x))/k_B T.$$

The final system of equations written in dimensional variables, which we solved numerically has the following form:

$$\begin{aligned} \frac{d^2 \Phi(X)}{dX^2} &= 1 - N'_c F_{1/2}(\xi_n(X) - \Phi(X)) + \\ &+ N'_v F_{1/2}(\Phi(X) - \xi_p(X) - \xi_g) - R_0 r(X), \\ \frac{d\xi_n(X)}{dX} &= \frac{J_n(X)}{N'_c F_{1/2}(\xi_n(X) - \Phi(X))}, \\ \frac{d\xi_p(X)}{dX} &= \frac{\mu_n}{\mu_p} \frac{J_p(X)}{N'_v F_{1/2}(\Phi(X) - \xi_p(X) - \xi_g)}, \end{aligned}$$

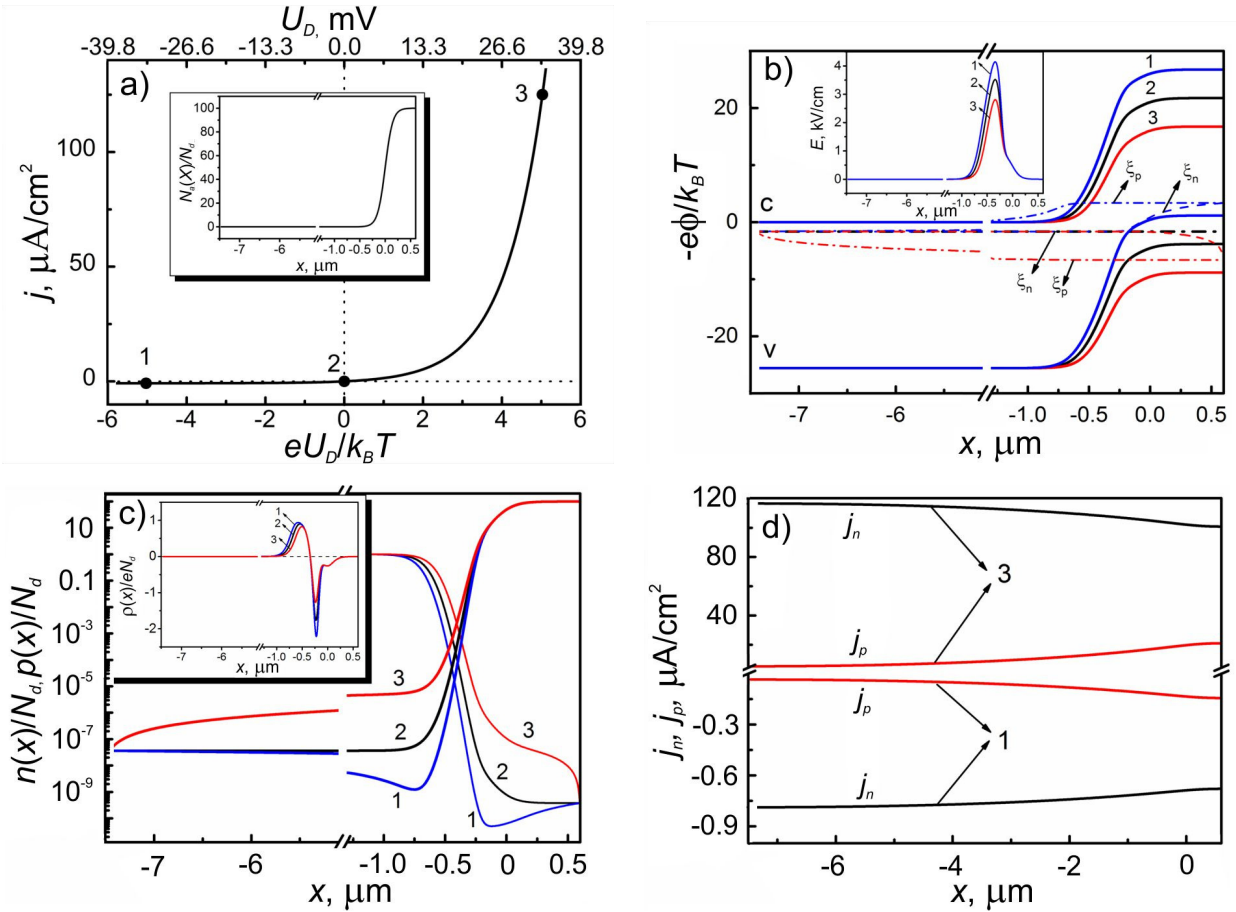


**Fig. 3.** Panel (a) shows the current-voltage characteristic; (b) non-equilibrium spatial distributions of the potential profile, including the quasi-Fermi levels of electrons (dashed lines) and holes (dash-dotted line); (c) non-equilibrium electron (thin lines) and hole (thick lines) concentrations and (d) electron and hole current densities. The insets in the panels (a), (b) and (c) depict the form of  $p$ -doping profile, electric field distribution and total charge density distribution, respectively. All the curves marked by 1, 2, 3 correspond to the three values of applied voltage  $U_D' = -5, 0, 5$  ( $-33, 0, 33$  mV), respectively.

$$\frac{dJ_n}{dX} = \Gamma [N'_c N'_v F_{1/2} (\xi_n(X) - \Phi(X)) \times F_{1/2} (\Phi(X) - \xi_p(X) - \xi_g) - N'(X) P'(X)],$$

$$\frac{dJ_p}{dX} = -\frac{dJ_n}{dX}, \quad (9)$$

where  $\xi_{n,p} = \epsilon_{n,p}/k_B T$ , dimensionless current densities  $J_{n,p} = j_{n,p}/J_d$  are scaled on characteristic current density,  $J_d = eN_d \mu_n E_d$ ; dimensionless coefficient of bulk recombination,  $\Gamma = eN_d L_d \gamma / \mu_n k_B T$  and  $N'(X), P'(X)$  are the dimensionless equilibrium electron and hole concentrations, respectively.

The system (9) should be supplied by the boundary conditions inherent for the Ohmic contacts:

$$\begin{aligned} \Phi(-L'_n) &= 0, \\ \Phi(-L'_p) &= \Phi_b - U_D', \\ \xi_e(-L'_n) &= \xi_p(-L'_n) = \xi_F, \\ \xi_e(-L'_p) &= \xi_p(L'_p) = \xi_F - U_D'. \end{aligned} \quad (10)$$

In Eqs. (10),  $\xi_F$  and  $\Phi_b$  are the equilibrium Fermi level and height of the electrostatic barrier that are obtained in the previous section.  $U_D' = eU_D/k_B T$  is the dimensionless applied voltage.

### 3.1. Current-voltage characteristics and profiles of non-equilibrium electrostatic characteristics

Using the results of Section 2 we developed the procedure of numerical solution of the BVP problem for the system (9) with the boundary condition (10). The procedure was applied to the calculations of  $I$ - $V$  characteristics,  $j(U_D)$ , as well as the spatial distributions of electric characteristics for the biased InSb  $p$ - $n$  diode with the following model parameters. The form of the  $p$ -doping profile,  $r(x)$ , is given by the function mentioned in the previous section with the parameter  $\alpha = 0.5$ . Dimensionless coordinates of the contacts:  $L'_n = -100$  ( $\sim -7.5 \mu\text{m}$ ) and  $L'_p = 8$  ( $\sim 0.6 \mu\text{m}$ ). In this case, the total width of the diode base is approximately  $8 \mu\text{m}$ . Like to the previous section, we set  $N_d = 10^{15} \text{ cm}^{-3}$ ,  $N_a = 10^{17} \text{ cm}^{-3}$  and  $T = 77 \text{ K}$ . The following values of the electron,  $\mu_n = 10^5 \text{ cm}^2/\text{V}\cdot\text{s}$ , hole,  $\mu_p = 10^3 \text{ cm}^2/\text{V}\cdot\text{s}$ , mobilities and the coefficient of bulk recombination,  $\gamma = 5 \cdot 10^{-8} \text{ cm}^3/\text{s}$ , were chosen as for the perfect InSb sample [12]. At these values, the dimensionless parameter,  $\Gamma = 4 \cdot 10^{-6}$ .

All the important electric characteristics of assumed  $p$ - $n$  diode are summarized in Figs 3a to 3d. Fig. 3a provides the result of calculations for current-voltage

characteristics inherent to the  $p$ - $n$  diode, neglecting the contribution of contact resistance. At assumed parameters, in forward bias,  $j(U_D)$  shows rapid exponential growth with typical values of 10...150  $\mu\text{A}/\text{cm}^2$  within the range of applied voltages 15...35 mV. In the reverse bias,  $j(U_D)$  is rapidly saturated and has the values less than  $-1 \mu\text{A}/\text{cm}^2$ . As seen from Figs 3b and 3c, the space charge region (depletion layer) of the diode has the width close to 1  $\mu\text{m}$ .

With increasing the forward bias, the bottom of the conduction band and top of the valence band (curves 3 in Fig. 3b) drops down, which leads to shrinking the depletion layer width and decreasing the amplitudes of the built-in electric fields (see inset in Fig. 3b) in comparison with unbiased case. Across the whole diode, the electron quasi-Fermi level lies above the quasi-Fermi level of holes. In the forward bias, electrons are injected to the  $p$ -region and holes are injected to the  $n$ -region, which is the result of considerable increasing the minor carrier concentrations. For example, at 33 mV the minor carrier concentration becomes one order larger than that at equilibrium (Fig. 3c). At the same time, the major carrier concentration in the corresponding regions remains practically the same as in the equilibrium state.

In the reverse biased diode (see curves 1), the situation is opposite, *i.e.*, the conduction and valence bands are ascended, built-in electric field is increased, depletion layer is broadened with decreasing the minor carrier concentrations. Also, the positions of the quasi-Fermi levels are reversed. The hole quasi-Fermi level lies above the electron one.

Fig. 3d illustrates spatial distributions of the partial currents corresponding to the electron and hole flows. As seen, both electron,  $j_n$ , and hole,  $j_p$ , currents demonstrate a weak spatial dependence in the space charge region and remain almost constant in the quasi-neutral regions. For both signs of the applied voltage, the amplitude of  $|j_n|$  decreases and amplitude of  $|j_p|$  increases while moving from the left side ( $n$ -doped region) to the right side ( $p$ -doped region) of the sample. Also, we found that currents corresponding to the minor carrier concentrations (current  $j_n$  in the  $p$ -doped region and current  $j_p$  in the  $n$ -doped region) have dominating diffusive components.

At the assumed parameters, the electron current dominates over the hole current. This observation corresponds to the geometry of the diode, in which the right quasi-neutral region is much shorter than the carrier diffusion lengths.

Indeed, the obtained results of the numerical calculations are well-agreed with the known physics of the  $p$ - $n$  diode. However, the analysis of the obtained results should be supported by estimations of the characteristic length and comparison with phenomenological transport theory of the  $p$ - $n$  junction [32, 33]. The *standard* model that describes diffusive mechanism of the current flowing through the  $p$ - $n$  junction gives the following form of  $I$ - $V$  characteristics:  $j = j_s [\exp(eU_D/k_B T) - 1]$ , with  $j_s$  being the dark saturation current density. The saturation current density

$j_s = e [D_n n_p / W_{n,D} + D_p p_n / W_{p,D}]$  where  $n_p$  and  $p_n$  are minor electron and hole concentrations,  $W_{n,D}$  and  $W_{p,D}$  – electron and hole diffusion lengths, respectively. Diffusion lengths depend on the parameter  $\gamma$ , values of major electron,  $n_n$ , and hole,  $p_p$ , concentrations, and they are given by the following expressions:

$$W_{n,D} = \sqrt{D_n / \gamma p_p} \quad \text{and} \quad W_{p,D} = \sqrt{D_p / \gamma n_n}.$$

The denominators in the latter formulae correspond to the electron lifetime in  $p$ -region,  $\tau_n = 1/\gamma p_p$  and hole lifetime in the  $n$ -region,  $\tau_p = 1/\gamma n_n$ . The numerical calculation gives the following values:  $p_p = p(L_p) \approx 10^{17} \text{ cm}^{-3}$ ,  $n_n = n(L_n) \approx 10^{15} \text{ cm}^{-3}$ ,  $n_p = n(L_p) \approx 3.8 \cdot 10^5 \text{ cm}^{-3}$ ,  $p_n = p(L_n) \approx 3.65 \cdot 10^7 \text{ cm}^{-3}$ . Using the Einstein relationship (assuming Boltzmann statistics), we obtained that  $D_{n,p} = 660, 6.6 \text{ cm}^2/\text{s}$  and  $W_{n,D} \approx W_{p,D} = 3.6 \mu\text{m}$ . The obtained values of the diffusion lengths are the same order of the width of depletion layer ( $\sim 1 \mu\text{m}$ ) and much higher than the size of  $p$ -doped (right quasi-neutral) region. The estimation gives the saturation current density  $j_s = 0.2 \mu\text{A}/\text{cm}^2$ . The obtained value of  $j_s$  is in five times less than that obtained in the numerical calculations. The main reason of this mismatch is the result of the chosen values of diode's parameters. The *standard* model was developed under assumption of the Boltzmann statistics of the carriers, narrow depletion layer (much shorter than the diffusion lengths) and for infinitely-long quasi-neutral regions. Here, we considered the case of a *short* diode with a relatively long depletion region and relatively short quasi-neutral regions. Moreover, we took into account the possible carrier degeneracy and specific form of the  $p$ -doping profile. The latter is beyond the frames of the *standard* model for the  $p$ - $n$  junction.

Finally, we investigated modified  $I$ - $V$  characteristics versus recombination rates (Fig. 4a) and  $p$ -doping level (Fig. 4b).

In Figs. 4, the  $I$ - $V$  characteristics are presented in the convenient form of the logarithmic scale and for absolute values of the currents. As seen, the  $I$ - $V$  characteristics crucially depend on electron-hole recombination rate. The currents are progressively increasing with an increasing of the parameter  $\gamma$ . The obtained numerical values of the saturated dark currents,  $\bar{j}_s \sim \sqrt{\gamma}$ . We ascertained that  $I$ - $V$  characteristics obtained numerically can be approximated with great precision by the asymptotic expression:  $j = \bar{j}_s [\exp(eU_D/k_B T) - 1]$ . The results given by the latter formula are shown in Fig. 4a by dashed curves. The visible deviation between exact calculations and approximations is observed only at largest recombination parameters  $\gamma = 5 \cdot 10^{-4} \text{ cm}^3/\text{s}$ . At this parameter, the slope of  $I$ - $V$  characteristics for the forward bias is less than 1. It is agreed with the model of the  $p$ - $n$  diode with the wide depletion region (much longer than the diffusion lengths) and high injection currents. In the frames of the latter analytical model,  $I$ - $V$  characteristic obeys the following formula  $j = \bar{j}_s [\exp(eU_D/2k_B T) - 1]$  [26].

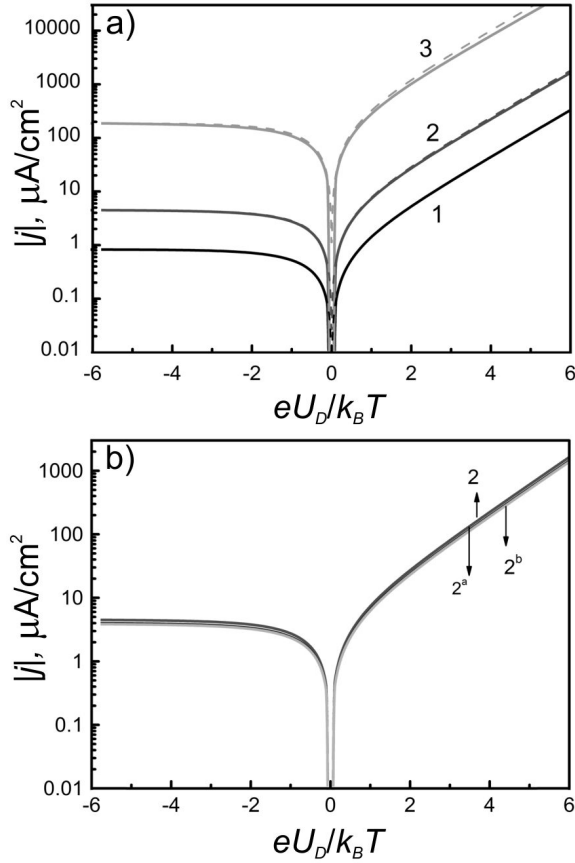


**Fig. 4.** Panel (a): solid curves 1, 2, 3 are the  $I$ - $V$  characteristics,  $|j|(U_D)$ , for different parameters of  $\gamma = 5 \cdot 10^{-8}$ ,  $5 \cdot 10^{-6}$ ,  $5 \cdot 10^{-4} \text{ cm}^3/\text{s}$ , respectively. The dashed curves are the results of the approximate calculations mentioned in the text. Panel (b):  $I$ - $V$  characteristics,  $|j|(U_D)$ , for  $\gamma = 5 \cdot 10^{-6} \text{ cm}^3/\text{s}$  and for  $N_a = 10^{17}$ ,  $5 \cdot 10^{17}$ ,  $2 \cdot 10^{18} \text{ cm}^{-3}$  (curves 2, 2<sup>a</sup>, 2<sup>b</sup>, respectively). The other parameters are the same as for Fig. 3a.

Fig. 4b demonstrates the weak dependence of  $I$ - $V$  characteristics vs concentration of  $p$ -doping at the same other parameters.

The proposed transport theory, without any simplification, properly describes behavior of the electric characteristics of the  $p$ - $n$  diode under the external bias including the  $I$ - $V$  characteristics in the frames of the classic transport picture. However, there are at least two effects remaining beyond our transport model and which can be important for the diodes with heavy  $p$ -doping. Both can considerably increase the dark currents. The first one is the tunneling effect. As seen from Fig. 3b, even at  $U_D \sim 30 \text{ mV}$ , the bottom of the conduction band in the  $n$ -region almost coincides with the top of the valence band in the  $p$ -region. It can facilitate the flow of the tunneling current. The second effect is strong built-in electrostatic fields of the order of several  $\text{kV}/\text{cm}$  (see inset in Fig. 3b). At these fields, the breakdown effects can occur (for InSb, the breakdown fields are of the same order [12]), which can initiate avalanche current at moderate reverse biases.

The developed numerical procedure of the calculations for  $I$ - $V$  characteristics was applied to the analysis of the InSb  $p$ - $n$  diode fabricated in ISP Labs.

#### 4. Fabrication of the InSb photodiode under the test

The  $n$ -type InSb wafers with thickness  $500 \mu\text{m}$  and doped by Te impurities with sheet electron concentration of  $(0.8 \dots 2) \cdot 10^{14} \text{ cm}^{-2}$  (corresponding bulk concentrations are  $(1.6 \dots 4) \cdot 10^{15} \text{ cm}^{-3}$ ) were chosen as initial core element to fabricate the photodiode. The surface treatment was carried out by the supplier of the original plates, and the plates were delivered in vacuum packages. Formation of  $p$ - $n$  junction was performed in two stages by ion implantation of  $\text{Be}_9^+$  ions on the whole surface. The beam with ion fluxes up to  $10^{14} \text{ cm}^{-2}$  and ion energies  $40 \text{ keV}$  was used at the first stage. The beam with ion fluxes  $5 \cdot 10^{13} \text{ cm}^{-2}$  and energies of  $100 \text{ keV}$  was used at the second stage.

Then, the mesa structure with the depth of  $1.3 \dots 1.7 \mu\text{m}$  was formed by contact photolithography and liquid etching of InSb in  $\text{HF}:(\text{COOH})_2:\text{H}_2\text{SO}_4:\text{H}_2\text{O}_2 = 20:8:20:1$  etchant. The depth of the mesa structure was chosen as based on the guaranteed removal of the  $\text{Be}_9^+$ -doped InSb layer from the original structure in the passive regions of the photodiode. Photoresist was removed by boiling in acetone. The two-stage rapid thermal annealing was used to activate the implanted impurities. The first stage includes annealing at  $280 \text{ }^\circ\text{C}$  for  $120 \text{ s}$ ; the second one includes annealing at  $380 \text{ }^\circ\text{C}$  for  $20 \text{ s}$ . Heating the InSb plate was carried out at the speed close to  $50 \text{ }^\circ\text{C}/\text{s}$  with further cooling at the speed  $0.2 \text{ }^\circ\text{C}/\text{s}$ . Before the heat treatment, the plate was subjected to chemical purification in  $\text{NH}_4\text{OH}:\text{H}_2\text{O}_2 = 1:1$ , washed in deionized water and dried in a centrifuge with dry nitrogen.

Then, the near-surface region of the plate was cleaned by successive anodizing in an electrolyte of the composition (wt.%):  $(\text{CH}_3)_2\text{NC}(\text{O})\text{H} - 70$ ,  $(\text{NH}_4)_2\text{S}_2\text{O}_8 - 0.5$ ,  $(\text{NH}_4)\text{F} - 0.005$ ,  $\text{C}_3\text{H}_5(\text{OH})_3 - 29.495$  in two regimes. The first regime was galvanostatic in the electrolytic InSb-Pt cell with a gap between the electrodes of  $1 \text{ cm}$  at a constant current density  $50 \mu\text{A}/\text{cm}$  (the process continues until the voltage between the electrodes reach the value of  $10 \text{ V}$ ). Second regime was voltstatic with a constant voltage between the electrodes of  $10 \text{ V}$  (the process continues until the current density reaches the value of  $0.5 \mu\text{A}/\text{cm}$ ). The next cleaning process includes removal of anodic oxide (AO) in the solution of buffered oxide etchant in  $1:10$  deionized water; sulfating of the surface in a  $1 \text{ M}$  aqueous solution of  $\text{Na}_2\text{S}$  for  $3 \text{ min}$  at  $40 \text{ }^\circ\text{C}$ ; removing the residual oxides of InSb in solution of  $\text{HCl}:\text{H}_2\text{O} = 1:10$  with following washing in deionized water and boiling in isopropanol to remove residual water from the surface of the plate.

Before formation of the annular contacts, the passivating, antireflective layer of  $\text{SiN}_x$  with the thickness  $220 \text{ nm}$  was deposited onto surface, using the plasma-enhanced chemical vapor deposition from the gas-vapor mixture  $(\text{SiH}_4 + \text{NH}_3 + \text{N}_2)$  at  $300 \text{ }^\circ\text{C}$ . The annular contacts were formed by contact photolithography and liquid selective etching of  $\text{SiN}_x$  to the InSb in the solution of buffered oxide etchant. Before

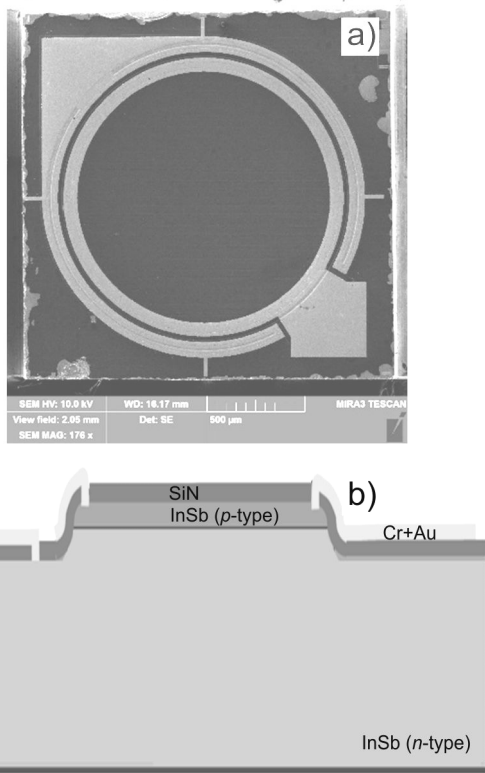


**Fig. 5.** Picture of Be-ion implanted  $p$ - $n$  InSb diode (top) and sketch of transversal geometry of the photodiode. The size of mesa structure is equal to 1.47 mm, the size of active region of the photodiode is 1.3 mm.

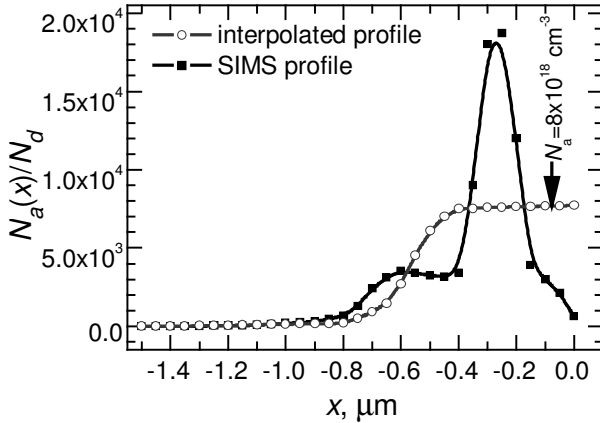


**Fig. 6.** The  $p$ -type doping profile extracted from SIMS measurements. The form of the interpolated profile is used in the calculations.

metal deposition, the photoresist was removed using acetone, with following cleaning the surface in the solution of HCl:acetone = 1:10. Covering with Cr metal layer of the thickness 40 nm and Au with 330-nm thickness was realized using the physical vapour deposition at 150 °C and a pressure in the operation chamber of no higher than  $5 \cdot 10^{-6}$  Pa. The metal contacts of the photodiode was formed using photolithography and sequential liquid etching of Au in the solution of 10 g KI + 2.5 g I<sub>2</sub> in 100 ml of H<sub>2</sub>O at 22 °C and Cr in solution of HCl: H<sub>2</sub>O = 2:1 at 60 °C. The photoresist was removed in acetone.

The picture of the final prepared for use photodiode together with the sketch of its transversal geometry is shown in Fig. 5.

The spatial profiles of the implanted Be-impurities were investigated using the Secondary Ion Mass Spectrometry (SIMS) techniques with the commercial setup Mass spectrometer “Atomika 4000”. The SIMS-profiles were recorded before and after the thermal annealing and they did not show the essential difference. The obtained profile of implanted Be-impurities is shown in Fig. 6.

## 5. Calculated and measured I-V characteristics

The calculations of the  $I$ - $V$  characteristics for the interpolated  $p$ -doping profile (solid curve in Fig. 6) were performed in the frames of the transport model discussed in Section 3. However, here we took into account the dependence of the electron and hole lifetimes  $\nu$ s respective carrier concentrations, being based on the literary data [6]. Fig. 7a presents the electron,  $\tau_n$ , and hole,  $\tau_p$ , lifetimes as functions of the relative distance between the equilibrium Fermi level and top of the valence band. Having the potential profile (Fig. 7b) and electron, and hole concentrations (Fig. 7c) obtained under the equilibrium condition, we calculated spatial distributions of the parameters

$\gamma_n(x) = [\tau_p (\xi_F + \xi_g - \Phi(x)) n(x)]^{-1}$  and  $\gamma_p(x) = [\tau_n (\xi_F + \xi_g - \Phi(x)) p(x)]^{-1}$  that are the recombination coefficients in  $n$ - and  $p$ -regions, respectively. In the calculations of the  $I$ - $V$  characteristics, we used single  $\gamma(x)$  (see Fig. 7d), which is the result of the following interpolation:  $\gamma(x) = \gamma_n(x)$  at  $x < x_{ch}$  and  $\gamma(x) = \gamma_p(x)$ , where  $x_{ch}$  is the coordinate corresponding to the equality of  $\gamma_p(x_{ch}) = \gamma_n(x_{ch})$ . As seen, this interpolation gives practically constant values of  $\gamma(x)$  in the  $n$ - and  $p$ -regions ( $\gamma \approx 10^{-9}$  and  $\gamma \approx 3 \cdot 10^{-10}$  cm<sup>3</sup>/s, respectively) and considerable increasing the recombination coefficient (up to  $10^{-5}$  cm<sup>3</sup>/s) in the depletion region. The results in Fig. 7 were obtained for the total diode length,  $L = 50 \mu\text{m}$ . The diode under test had the full width of  $500 \mu\text{m}$ . However, we checked that the further increase in  $L_D$  no longer affects on dependence of  $j(U_D)$  but essentially increases the computational time. Moreover, the remained quasi-neutral  $n$ -doped region can be treated as the part of the contact resistance,  $R_c$ .

The latter can be estimated from the analysis of the measured  $I$ - $V$  characteristic at the forward bias. Typically, at high forward biases the observed  $I$ - $V$  characteristics of  $p$ - $n$  diode show the linear behavior with the slope corresponding to  $R_c$ . This situation occurs when the region of  $p$ - $n$  junction already has the resistance lower than that of wide quasi-neutral regions including Ohmic contacts. From the measured  $I$ - $V$  characteristics (dotted curve in Fig. 8), we found that  $R_c = 72 \text{ Ohm}$ .

The latter can be estimated from the analysis of the measured  $I$ - $V$  characteristic at the forward bias. Typically, at high forward biases the observed  $I$ - $V$  characteristics of  $p$ - $n$  diode show the linear behavior with the slope corresponding to  $R_c$ . This situation occurs when the region of  $p$ - $n$  junction already has the resistance lower than that of wide quasi-neutral regions including Ohmic contacts. From the measured  $I$ - $V$  characteristics (dotted curve in Fig. 8), we found that  $R_c = 72 \text{ Ohm}$ .

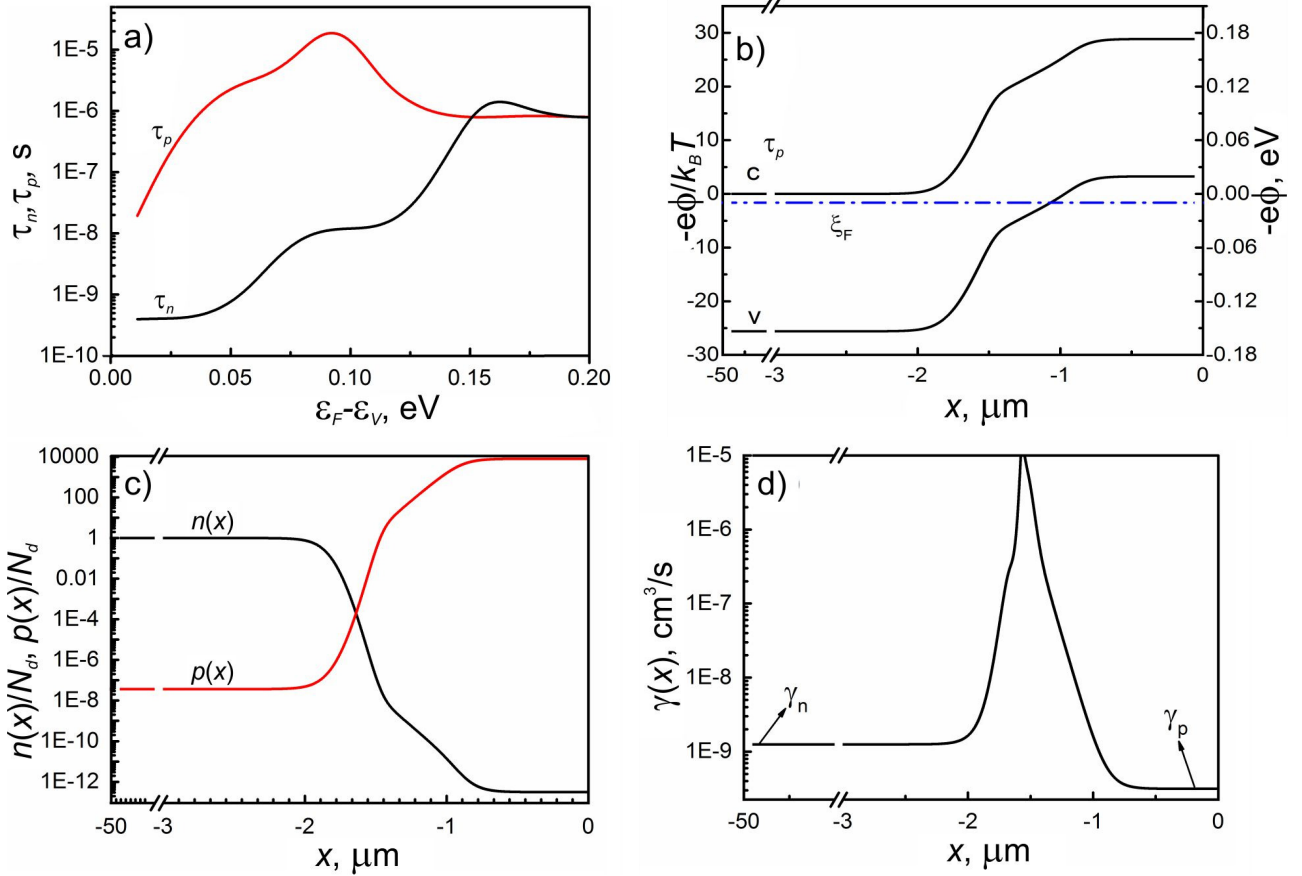


**Fig. 7.** Panel (a): electron and hole lifetimes. Panel (b): spatial distribution of the equilibrium electrostatic profile and Fermi level (dash-dotted line) calculated for the doping profile presented in Fig. 6. Panel (c): equilibrium electron and hole distributions. Panel (d): distribution of the recombination coefficient values.

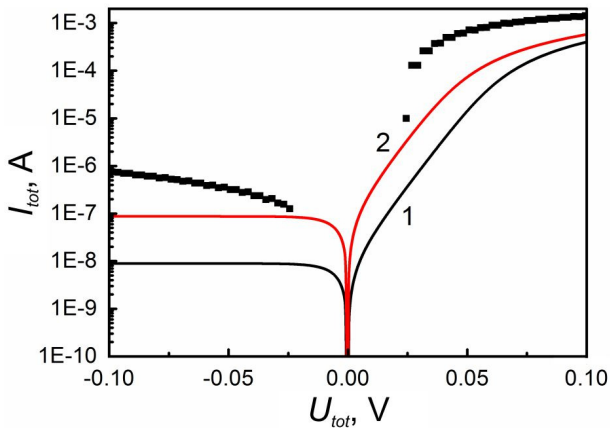


**Fig. 8.**  $I$ - $V$  characteristics of the InSb p-n diode. The dotted curves are the result of measurements at  $T = 77$  K. Solid curves are the results of the calculations of dependence  $I_{tot}(U_{tot})$ . The curve 1 corresponds to the recombination coefficient depicted in Fig. 7d. The curve 2 corresponds to  $\gamma$  100 times larger than that for the curve 1.

For comparison, we also estimated the resistance,  $R_a$ , of the InSb  $n$ -doped wafer before  $p$ -doping processing, as follows:  $R_a = L/eN_d\mu_e S$ , with  $S$  being current collected area. For  $L = 500 \mu\text{m}$ ,  $S = 0.013 \text{ cm}^2$  (corresponding diameter of  $0.13 \text{ cm}$ ),  $N_d = 10^{15} \text{ cm}^{-3}$ ,  $\mu_e = 10^5 \text{ cm}^2/\text{V}\cdot\text{s}$  the estimations gives  $R_a = 0.23 \text{ Ohm}$ , which is much less than  $R_c$ . Thus, using the dependence  $j_D(U_D)$  we calculated  $I$ - $V$  characteristic (solid curves in Fig. 8) in terms of total current flowing through the

diode,  $I_{tot}$ , and the total applied bias,  $U_{tot}$ , where  $U_{tot} = jS$  and  $U_{tot} = U_D + R_c I_{tot}$ .

The developed theory just qualitatively describes the measured characteristics. For this, there are several reasons that relates to both frames of the developed theory and quality of the sample. As seen, the theory predicts saturation of the dark current starting at  $U_{tot} \sim 0.02 \text{ V}$ . Instead of that, the experiment shows the growth that can be associated with tunneling effect through the space charge region or electrical avalanche effects due to strong built-in electric fields in this region. Also, the current leakage effects can be important. On the other hand, this theory is developed for the perfectly Ohmic contacts and one-dimensional geometry of the sample. In practice, sample has two-dimensional geometry in the sense of electrostatics. The injection properties of the contacts should be also tested.

## 6. Conclusions

In summary, we developed the transport model and efficient numerical algorithms for calculations of the basic electric characteristics of p-n diode with spatially non-uniform p-doping profiles. The model properly describes the diffusive and generation-recombination mechanisms of current flow through the diode. The model has also taken into account the arbitrary degeneracy of the carriers and possible non-uniform distribution of the bulk recombination coefficient in the different regions of the p-n diode. We have ascertained

that the non-uniform profile of  $p$ -doping can lead to formation of the  $p$ - $n$  junction with a specific two-slope form of the electrostatic barrier and two regions with the high built-in electric fields. We have found that at strong  $p^+$ -doping the band structure of the InSb  $p$ - $n$  junction has the form capable to facilitate the emergence of additional mechanisms of current flow due to the tunneling and avalanche effects at the reverse bias. Using the literary data of the electron and hole lifetimes in InSb at cryogenic temperatures, we found that the coefficient of the bulk recombination can have the essential spatial dependence and considerably increases in the space charge region of  $p$ - $n$  diode. The developed theory was adopted and applied to the analysis of  $I$ - $V$  characteristic of Be-ion implanted  $p$ - $n$  InSb diode fabricated in Labs of ISP. Fabrication technology, including details of the implantation, processing and testing have been widely discussed. Performed calculations have predicted the values of dark currents of order of  $0.01 \dots 1 \mu\text{m}$ , which is at least 1-2 orders less than those observed in measurements. Moreover, the measured  $I$ - $V$  characteristics have shown the weak growth at the reverse bias, instead of saturation. It can be associated with the existence of additional current mechanisms, namely: tunneling effect and the avalanche one. The performed calculations of the band structures of the biased  $p$ - $n$  diode with the set parameter of ion implantation indicate the possibility of the existence of these mechanisms.

The proposed transport theory of  $p$ - $n$  diode will be improved and in what follows developed to the studies of the photovoltaic characteristics. It has been planned to develop the theory that will self-consistently includes electron transport and electrodynamic simulations. The planned theory will be focused on the study of the photodiodes incorporated with plasmonic elements.

### Acknowledgement

This work is partially supported by the Ministry of Education and Science of Ukraine (Project M/24-2018) and German Federal Ministry of Education and Research (BMBF Project 01DK17028).

### References

1. Rogalski A. Infrared detectors for the future. *Acta Physica Polonica A*. 2009. **116**, No 3. P. 389–405.
2. Downs Chandler and Vandervelde Thomas E. Progress in infrared photodetectors since 2000. *Sensors* (Basel). 2013. **13**, No 4. P. 5054–5098.
3. Karim Amir and Andersson Jan Y. Infrared detectors: Advances, challenges and new technologies. *IOP Conf. Ser.: Mater. Sci. Eng.* 2013. **51**. P. 012001.
4. Hilsum C. and Rose-Innes A.C. *Semiconducting III-V Compounds*. New York, Macmillan (Pergamon), 1961.
5. Rode D. L. Electron transport in InSb, InAs, and InP. *Phys. Rev. B*. 1971. **3**, No 10. P. 3287–3299.
6. Laff R.A. and Fan H.Y. Carrier lifetime in indium antimonide. *Phys. Rev.* 1961. **121**, No 1. P. 53–62.
7. Wampler W.R. and Springford M. The lifetime of electrons in InSb, studied using the de Haas-van Alphen effect. *J. Phys. C: Solid State Phys.* 1972. **5**. P. 2345–2356.
8. Zitter R.N., Strauss A.J., and Attard A.E. Recombination processes in  $p$ -type indium antimonide. *Phys. Rev.* 1959. **115**, No 2. P. 266–273.
9. Pines M.Y. and Stafsudd O.M. Recombination processes on intrinsic semiconductors using impact ionization capture cross sections in Indium Antimonide and Mercury Cadmium Telluride. *Infrared Phys.* 1980. **20**. P. 73–91.
10. Rogalski A. and Orman Z. Band-to-band recombination in  $\text{InAs}_{1-x}\text{Sb}_x$ . *Infrared Phys.* 1985. **25**, No 3. P. 551–560.
11. Liu P.Y. and Maan J.C. Optical properties of InSb between 300 and 700 K. I. Temperature dependence of the energy gap. *Phys. Rev. B*. 1993. **47**. P. 16274.
12. Levinstein M., Rumyantsev S. and Shur M. *Handbook Series on Semiconductor Parameters* (Vol. 1). World Scientific, 1996.
13. Adachi S. *Group-IV, III-V and II-VI Semiconductors*. Wiley, 2005.
14. Foyt A.G., Lindley W.T., and Donnelly J.P.  $n$ - $p$  junction photodetectors in InSb fabricated by proton bombardment. *Appl. Phys. Lett.* 1970. **16**. P. 335.
15. Hurwitz C.E. and Donnelly J.P. Planar InSb photodiodes fabricated by Be and Mg ion implantation. *Solid-State Electronics*. 1975. **18**. P. 753–756.
16. Bogatyriov V.A., Kachurin G.A. and Smirnov L.S. Properties of InSb  $p$ - $n$  junctions fabricated by Zn implantation with subsequent drive-in diffusion. *Radiation Effects*. 1980. **49**, No 1-3. P. 45–49.
17. Liu J. Rapid thermal annealing characteristics of Be implanted into InSb. *Appl. Surf. Sci.* 1998. **126**. P. 231–234.
18. Goltvyanskyi Yu.V., Gudymenko O.J., Dubikovskiy O.V., Liubchenko O.I., Oberemok O.S., Sabov T.M., Sapon S.V., Chunikhina K.I. Investigation of photodiode formation processes in InSb by using beryllium ion implantation. *Optoelectronics and Semiconductor Technique*. 2017. **52** (in Ukrainian).
19. Abautret J., Perez J.P., Evirgen A., Rothman J., Cordat A., and Christol P. Characterization of midwave infrared InSb avalanche photodiode. *J. Appl. Phys.* 2015. **117**. P. 244502.
20. Gunapala S.D., Bandara S.V., Rafol S.B., and Ting D.Z. Chapter 2 – Quantum well infrared photodetectors. *Semiconductors and Semimetals*. 2011. **84**. P. 59–151.
21. Liu H.C. Quantum dot infrared photodetector. *Opto-Electron. Rev.* 2003. **11**, No 1. P. 1–5.
22. Mitin V.V., Kochelap V.A., and Strosio M. *Quantum Heterostructures for Microelectronics and Optoelectronics*. Ch.12. New York, Cambridge University Press, 1999.

23. Shadrin V.D., Mitin V., Choi K., Kochelap V.A. Photoconductive gain and generation-recombination noise in quantum-well photodetectors biased to strong electric field. *J. Appl. Phys.* 1995. **78**, No 9. P. 5765–5774.
24. Bonakdar A. and Mohseni H. Impact of optical antenna and plasmonics on infrared imagers. *Infrared Physics & Technology*. 2013. **59**. P. 142–145.
25. Rosenberg J., Sheno R.V., Krishna S. and Painter O. Design of plasmonic photonic crystal resonant cavities for polarization sensitive infrared photodetectors. *Opt. Exp.* 2010. **18**, No 4. P. 3672.
26. Hopkins F.K. and Boyd J.T. Dark current analysis of InSb photodiodes. *Infrared Phys.* 1984. **24**, No 4. P. 391–395.
27. Tai-Ping Sun and Si-Chen Lee. The current leakage mechanism in InSb  $p^+n$  diodes. *J. Appl. Phys.* 1990. **67**. P. 7092.
28. BenDaniel D.J. and Duke C.B. Space-Charge Effects on Electron Tunneling. *Phys. Rev.* 1966. **152**, No 29. P. 683–692.
29. Banerjee K., Huang J., and Ghosh S. Modeling and simulation of long-wave infrared InAs/GaSb strained layer superlattice photodiodes with different passivants. *Infrared Phys. Technol.* 2011. **54**. P. 460.
30. Nadimi M. and Sadr A. Computer modeling of MWIR homojunction photodetector based on indium antimonide. *Adv. Mater. Res.* 2012. **383**. P. 6806.
31. Kruse P.W. Chapter 2 – Indium antimonide photoconductive and photoelectromagnetic detectors. *Semiconductors and Semimetals*. 1970. **5**. P. 15–83.
32. Anselm A. *Introduction to Semiconductor Theory*. Moscow, Nauka, 1978 (in Russian).
33. Bonch-Bruyevich V.L. and Kalashnikov S.G. *Semiconductor Physics*. Moscow, Nauka, 1977 (in Russian).